Analysis on the Magnetic Field Response for Nuclear Spin Co-Magnetometer Operated in Spin-Exchange Relaxation-Free Regime

WENFENG FAN[1], WEI QUAN[1,2,3,4], WEIJIA ZHANG[1], LI XING[1], AND GANG LIU[1,2,3]

[1]School of Instrumentation and Optoelectronic Engineering, Beihang University, Beijing 100191, China
[2]Innovative Research Institute of Frontier Science and Technology, Beihang University, Beijing 100191, China
[3]Advanced Innovation Center for Biomedical Engineering, Beihang University, Beijing 100191, China
[4]Beijing Academy of Quantum Information Sciences, Beijing 100191, China

Corresponding authors: Wei Quan (quanwei@buaa.edu.cn) and Gang Liu (lgang@buaa.edu.cn)

ABSTRACT A nuclear spin co-magnetometer operated in the spin-exchange relaxation-free (SERF) regime is a promising tool for long-term navigation application for its abilities to sense inertial rotation and to suppress environmental magnetic field disturbance. The magnetic field response model of a K-Rb-^{21}Ne nuclear spin co-magnetometer is derived based on the state space method and the model is experimentally validated on a tabletop SERF co-magnetometer. The theoretical and experimental results indicate that the relaxation rate of the nuclear spins limits the field-suppression ability. The results here not only give insight into the nature of self-compensate characteristic but also provide a precise model for the estimation of the magnetic noise-induced rotation measurement error in a SERF co-magnetometer.

INDEX TERMS Nuclear spin co-magnetometer, SERF, magnetic response model, magnetic noise induced error.

I. INTRODUCTION

Co-magnetometers first introduced in [1] are a series of magnetometers using at least two spin species with different gyromagnetic ratios occupying the same volume. As experiments relying on spin-dependent interactions are usually limited by noise and systematic effects induced by magnetic field, the co-magnetometer arrangement could be utilized to cancel the magnetic field dependence. Experiments benefit from this cancelation range from searches for electric dipole moments of neutron [2], searches for violation of local Lorentz invariance [3], [4] and for new spin-dependent forces [5], [6]. The co-magnetometer scheme also finds practical applications in high precision inertial rotation sensing, including the nuclear magnetic resonance gyroscope based on nuclear magnetic resonance technologies [7]–[11] and spin-exchange relaxation-free co-magnetometer (SERFCM) operated in SERF regime [12], [13].

The first SERFCM based on a K-^{3}He co-magnetometer was introduced by the Romalis group at Princeton University

in 2005 [13], and it features a higher sensitivity than nuclear magnetic resonance gyroscope as spin-exchange collisions do not broaden the magnetic resonance linewidth. In addition, it has a self-compensate characteristic as the noble gas magnetization follows the low frequency magnetic field fluctuations. In the case of a low frequency transverse magnetic field perturbation, the noble gas spins quickly settle to align with the total applied field. The transverse magnetization of noble gas spins cancels the perturbation, so the alkali-metal atoms feel no magnetic field change. However, the noble gas spins cannot cancel longitudinal perturbation. This is not a problem because the alkali-metal atomic magnetometer is inherently insensitive to longitudinal fields. For analytical solutions, the readers can refer to [12]. At the same time, the ultra-sensitive rotation measurement ability is still retained. The reported sensitivity and angle drift were 5×10^{-7} rad/s/Hz$^{1/2}$ and 0.04 °/h respectively. Our team developed a SERFCM based on a Cs-^{129}Xe co-magnetometer and analyzed its dynamics in [14] and [15]. In the next decade, much efforts were devoted to inertial rotation sensing theory analysis [16], dual-axis cross-talk decoupling scheme study [17], [18] and novel atom manipulation and interrogation methods

validation [19], [20]. As the gyromagnetic ratio of a ^{21}Ne atom is much smaller than that of a ^{3}He atom or a ^{129}Xe atom, the fundamental rotation measurement sensitivity of a K-Rb-^{21}Ne co-magnetometer is estimated to be higher than that of a K-^{3}He co-magnetometer or a Cs-^{129}Xe co-magnetometer at the same magnetic field noise level. Therefore, we have turned from Cs-^{129}Xe to K-Rb-^{21}Ne. Although a better sensitivity of 2.1×10^{-8} rad/s/Hz$^{1/2}$ has been achieved with various noises in the co-magnetometer suppressed [21], the low-frequency angle drift is only on par with that of Romalis group [13], [19]. The long-term stability of the co-magnetometer improved little even though we reduce it to tabletop instrument size with a volume of 350 mm × 350 mm × 280 mm to suppress the temperature induced drifts from optical components. It is not until the discovery of the influence of magnetic fields on the bias stability [22] that we realized the magnetic noise may set a limit on the performance of the co-magnetometer. This inspires us to seek methods for magnetic influence suppression by studying the mechanism of the magnetic field response.

In this paper, the magnetic field response model of the SERFCM is derived based on state space method and the model is experimentally validated on a tabletop K-Rb-^{21}Ne co-magnetometer. We find that the transfer function between the low frequency transverse magnetic field and system output can be characterized with first order differentiation element instead of differentiation element, which means that the nuclear magnetization can no longer be able to completely cancel the magnetic field fluctuations as supposed in previous works [13], [23]. Theoretical analysis on magnetic field transfer function models indicates that the discrepancy comes from the non-zero nuclear spin relaxation rate, which in former works was usually assumed to have a negligible impact on the field cancelation ability. The experimental results agree well with the theoretical simulation, implying the universal applicability of our model for magnetic response analysis in SERFCM. This model can be exploited to estimate the rotation measurement error induced by magnetic noise inherent in the magnetic shields, which, to our knowledge, has not been analyzed before.

II. THEORETICAL ANALYSIS

The complete behavior of the co-magnetometer can be approximated by a set of coupled Bloch equations for the electron and nuclear polarizations, $\boldsymbol{P}^e$ and $\boldsymbol{P}^n$ [13], [16]:

$$
\frac{\partial \boldsymbol{P}^e}{\partial t} = \frac{\gamma^e}{Q(P^e)} \left(\boldsymbol{B} + \lambda M^n \boldsymbol{P}^n + \boldsymbol{L} \right) \times \boldsymbol{P}^e - \boldsymbol{\Omega} \times \boldsymbol{P}^e
$$
$$
+ \frac{\left(R_p \boldsymbol{s}^p + R_{se}^{en} \boldsymbol{P}^n + R_m \boldsymbol{s}^m - R_{tot}^e \boldsymbol{P}^e \right)}{Q(P^e)}, \tag{1}
$$

$$
\frac{\partial \boldsymbol{P}^n}{\partial t} = \gamma^n \left(\boldsymbol{B} + \lambda M^e \boldsymbol{P}^e \right) \times \boldsymbol{P}^n - \boldsymbol{\Omega} \times \boldsymbol{P}^n
$$
$$
+ R_{se}^{ne} \boldsymbol{P}^e - R_{tot}^n \boldsymbol{P}^n. \tag{2}
$$

Here γ^e and γ^n are the gyromagnetic ratio of the electron and the nuclear spins. $Q(P^e)$ is the polarization-dependent

slowing-down factor of electron [24]. $\boldsymbol{B}$ is the ambient magnetic field, and $\boldsymbol{L}$ is the light shift experienced by the alkali-metal atoms. $\lambda M \boldsymbol{P}$ is the magnetic field produced by the magnetization of a spin ensemble in a spherical vapor cell, where M^e and M^n are the magnetization of electron and nuclear spins corresponding to full spin polarizations respectively, $\lambda = 8\pi\kappa_0/3$ is the geometrical factor containing the enhancement factor [25]. $\boldsymbol{\Omega}$ is the rotation rate vector. The total relaxation rate for electron spins is $R_{tot}^e = R_p + R_m + R_{sd}^e + R_{se}^{en}$, where R_p is the pumping rate from the pump beam, R_m is the pumping rate from the probe beam, R_{sd}^e is the spin-destruction rate, and R_{se}^{en} is the spin-exchange rate of the electron spins. $\boldsymbol{s}^p$ and $\boldsymbol{s}^m$ give the directions and magnitudes of the photon spin polarizations of the pump and probe laser beams. R_{tot}^n is the total relaxation rate of nuclear spins. $R_{tot}^n = R_{se}^{ne} + R_{sd}^n$, where R_{se}^{ne} is the spin-exchange rate of the nuclear spins, R_{sd}^n is the nuclear spin-destruction rate. In this paper, the z-axis is defined to be the direction of the pump laser, while the x-axis is defined as the direction of the probe laser. The longitudinal direction is referred to the direction along the z-axis, and the transverse direction is referred to the direction along the x- and y- axes.

To achieve the most sensitive rotation sensing ability, an external compensation field $B^c = -(B^n + B^e)$ along z-axis is employed to cancel the magnetic field produced by the magnetization of the nuclear- and electron-spin. Here $B^n = \lambda M^n P_0^n$ is the effective field from nuclear magnetization and $B^e = \lambda M^e P_0^e$ is the effective field from electron magnetization [13], [16]. P_0^n is the equilibrium value for the nuclear spin polarization along z-axis P_z^n, and P_0^e is the equilibrium value for the electron spin polarization along z-axis P_z^e. To study the responses of the spins under small transverse excitations, the magnitude of P_0^n and P_0^e are assumed to remain constant such that the polarization-dependent $Q(P^e)$ can also be assumed to be a stable value Q. The light shifts can be set to zero, thus $\boldsymbol{L} = \boldsymbol{0}$ [25]. Under these conditions, the system can be approximated as a linear time-invariant system and the system state equation can be written as

$$
\dot{\boldsymbol{X}} = \boldsymbol{A}\boldsymbol{X} + \boldsymbol{W}\boldsymbol{U}, \tag{3}
$$

where $\boldsymbol{X} = \left[P_x^e, P_y^e, P_x^n, P_y^n \right]^T$ is the state vector including the transverse components of electron and nuclear polarization, and $\boldsymbol{U} = \left[\Omega_x, \Omega_y, B_x, B_y \right]^T$ is the input vector including the applied transverse magnetic field and transverse rotation vector. And

$$
\boldsymbol{A} = \begin{bmatrix} \dfrac{-R_{tot}^e}{Q} & \dfrac{-\gamma^e \lambda M^e P_0^e}{Q} & \dfrac{R_{se}^{en}}{Q} & \dfrac{\gamma^e}{Q}\lambda M^n P_0^n \\[2ex] \dfrac{\gamma^e \lambda M^e P_0^e}{Q} & \dfrac{-R_{tot}^e}{Q} & \dfrac{-\gamma^e \lambda M^n P_0^n}{Q} & \dfrac{R_{se}^{en}}{Q} \\[2ex] R_{se}^{ne} & \gamma^n \lambda M^e P_0^e & -R_{tot}^n & -\gamma^n \lambda M^n P_0^n \\[2ex] -\gamma^n \lambda M^e P_0^e & R_{se}^{ne} & \gamma^n \lambda M^n P_0^n & -R_{tot}^n \end{bmatrix}, \tag{4}
$$

$$W = \begin{bmatrix} 0 & -P_0^e & 0 & \dfrac{P_0^e \gamma^e}{Q} \\[2mm] P_0^e & 0 & -\dfrac{P_0^e \gamma^e}{Q} & 0 \\[2mm] 0 & -P_0^n & 0 & P_0^n \gamma^n \\[2mm] P_0^n & 0 & P_0^n \gamma^n & 0 \end{bmatrix}. \tag{5}$$

The eigenvalues of matrix A is

$$\lambda_{1,2} = \Gamma_1 \pm i\omega_1$$
$$= \left(\alpha + \frac{\sqrt{\sqrt{a^2+b^2}+a}}{2\sqrt{2}} \right) \pm i \left(\beta - \frac{\sqrt{\sqrt{a^2+b^2}-a}}{2\sqrt{2}} \right), \tag{6}$$

$$\lambda_{3,4} = \Gamma_2 \pm i\omega_2$$
$$= \left(\alpha - \frac{\sqrt{\sqrt{a^2+b^2}+a}}{2\sqrt{2}} \right) \pm i \left(\beta + \frac{\sqrt{\sqrt{a^2+b^2}-a}}{2\sqrt{2}} \right). \tag{7}$$

Keeping the leading terms, the variables in (6) and (7) can be simplified to

$$\alpha = -\frac{R_{tot}^e}{2Q}, \tag{8}$$

$$\beta = \frac{\lambda M^e P_0^e \gamma^e + \lambda M^n P_0^n Q \gamma^n}{2Q}, \tag{9}$$

$$a = \left(\frac{R_{tot}^e}{Q} \right)^2, \tag{10}$$

$$b = \frac{2R_{tot}^e \left(-\lambda M^e P_0^e \gamma^e + \lambda M^n P_0^n Q \gamma^n \right)}{Q^2}. \tag{11}$$

Therefore, the dynamical response of the system contains two separate oscillations with different frequencies (imaginary part of the eigenvalues) and decay rates (real part of the eigenvalues).

Under zero initial conditions, we can obtain the transfer matrix of the system

$$G(s) = (sI - A)^{-1}B = N(s)/D(s), \tag{12}$$

where the numerator $N(s)$ is a 4×4 matrix, and the denominator

$$D(s) = \left[(s-\Gamma_1)^2 + \omega_1^2 \right] \left[(s-\Gamma_2)^2 + \omega_2^2 \right]. \tag{13}$$

At the typical working conditions of a SERFCM, the transfer function between B_x and P_x^e can be expressed as

$$G_{Bx}(s) = P_x^e(s)/B_x(s) = N_{13}(s)/D(s)$$
$$= \frac{K_{Bx}(s - z_{Bx1})(s - z_{Bx2})}{\left[(s-\Gamma_1)^2 + \omega_1^2 \right] \left[(s-\Gamma_2)^2 + \omega_2^2 \right]}, \tag{14}$$

where

$$K_{Bx} = -\frac{P_0^e \gamma^e \left(\lambda M^e P_0^e \gamma^e + \lambda M^n P_0^n Q \gamma^n \right)}{Q^2}, \tag{15}$$

and the two zero points of the transfer function (14) are

$$z_{Bx1} \approx -R_{tot}^n, \tag{16}$$

$$z_{Bx2} \approx \frac{-M^n P_0^n R_{tot}^e \gamma^n}{M^e P_0^e \gamma^e + M^n P_0^n Q \gamma^n}. \tag{17}$$

The transfer function between B_y and P_x^e is

$$G_{By}(s) = P_x^e(s)/B_y(s) = N_{14}(s)/D(s)$$
$$= \frac{K_{By}(s - z_{By1})(s - z_{By2})(s - z_{By3})}{\left[(s-\Gamma_1)^2 + \omega_1^2 \right] \left[(s-\Gamma_2)^2 + \omega_2^2 \right]}, \tag{18}$$

where

$$K_{By} = \frac{P_0^e R_{tot}^e \left(R_{tot}^n \right)^2 \gamma^e}{Q^2}, \tag{19}$$

and the three zero points of the transfer function (18) are

$$z_{By1} = \frac{-R_{tot}^e - QR_{tot}^n + \zeta}{2Q}, \tag{20}$$

$$z_{By2} \approx -R_{tot}^n, \tag{21}$$

$$z_{By3} = \frac{-R_{tot}^e - QR_{tot}^n - \zeta}{2Q}, \tag{22}$$

where

$$\zeta = \sqrt{4QR_{se}^{en}R_{se}^{ne} + \left(R_{tot}^e \right)^2 - 2QR_{tot}^e R_{tot}^n + Q^2 \left(R_{tot}^n \right)^2}. \tag{23}$$

According to the procedure described in [22], the compensation-point is found when the modulation of B_y does not affect the steady-state output of co-magnetometer. So it is a reasonable approximation that in (18) the zero point nearest to imaginary axis in complex plane z_{By1} equals to 0. Using (20), we can get

$$\zeta \approx R_{tot}^e + QR_{tot}^n. \tag{24}$$

Substituting (24) into (22), we can get

$$z_{By3} = -\frac{R_{tot}^e}{Q} - R_{tot}^n. \tag{25}$$

Compared with the results in [13] and [23], the analysis above indicates that the non-zero nuclear spin relaxation rate R_{tot}^n introduce another non-zero zero point in the magnetic field transfer functions, which aggravate the influence of the low frequency transverse magnetic field components.

III. EXPERIMENTAL RESULTS AND DISCUSSION

A tabletop K-Rb-^{21}Ne SERFCM was developed and used to verify the theoretical analysis. The schematic of the co-magnetometer is shown in Fig.1. The co-magnetometer contains a 10-mm-diameter spherical vapor cell with 1100 Torr of ^{21}Ne, 50 Torr nitrogen, and a droplet of natural abundance Rb with a mixture of K. The cell held in a boron-nitride oven is heated by ac current-driven heating coils. The temperature of the cell can be stabilized to any value between 160 °C and 200 °C by a PID control algorithm. The zero magnetic field operating condition of the co-magnetometer is provided via a tri-axial magnetic coil system within the
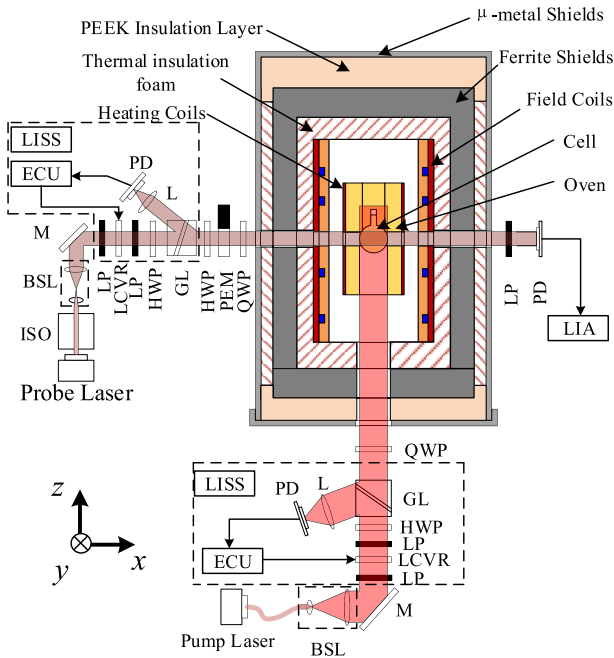
FIGURE 1. The schematic of the tabletop co-magnetometer. ISO: isolator, BSL: beam shaping lenses, M: reflection mirror, LP: linear polarizer, LCVR: liquid crystal variable retarder, HWP: half wave plate, GL: Glan-Prism, QWP: quarter wave plate, L: lens, PD: photodiode, PEM: photo-elastic modulator, LIA: lock-in amplifier, ECU: electronic control unit, LISS: laser intensity stabilization system. The LISS is used to guarantee the long-term stability of the intensity of the pump and probe lasers. A LISS mainly comprises of two crossed LPs, a LCVR, a HWP, a GL, a PD and an ECU. The output laser intensity of the LISS is monitored by the PD, which detects the intensity of a small portion of laser split by the GL. The PD signal is fed into the ECU. The ECU compares the current laser intensity with the set-point value and changes the driving voltage applied to the LCVR to change the output laser intensity.

FIGURE 2. T_1 time measurement of the longitudinal nuclear spin polarization of ^{21}Ne. The fitting curve (black line) indicates that T_1 is about 66 minutes with a cell temperature of 185 °C.

innermost shield. The shields are composed of one layer of 2 mm thick, high permeability μ-metal and a 6 mm thick, 60 mm inner-diameter ferrite shield. Thermal insulation foam is filled between layers to keep the temperature of the ferrite well below its Curie temperature of about 220 °C. K atoms are polarized along the z-axis by a fiber-introduced circularly polarized pumping beam. Rb atoms are polarized via the rapid spin exchange collisions between K and Rb atoms. Atomic spin precession of Rb atoms along the x-axis P_x^e is detected by the optical rotation of an off-resonant, linearly polarized light beam. Laser intensity stabilization systems are used to control the intensity of the pump and probe lasers. The polarization angles are precisely measured using a photo-elastic modulator [16] and a lock-in amplifier. For a simple and comprehensive description of the experiments, the conversion coefficient between P_x^e and the output voltage of the co-magnetometer is directly defined as K_{probe} here. The readers can refer to [26] and [27] for more detailed measurement principles.

We start by heating the cell to 185 °C and pumping the atoms for hours, the density ratio of K to Rb is estimated to be 1:110. During the optical pumping process, a holding longitudinal magnetic field is employed along z-axis to facilitate the polarization of ^{21}Ne. As is shown in Fig.2, the fitting
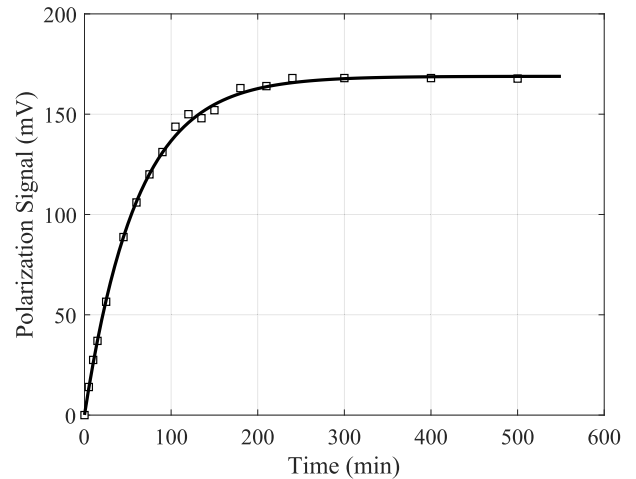
curve indicates that the longitudinal relaxation time T_1 of ^{21}Ne is about 66 minutes. After the polarization reaches the equilibrium state, the B_z field is set to the compensation point, making the co-magnetometer to sense the inertial rotation. And the scale factor of the co-magnetometer is calibrated as mentioned in our previous work [16].

To validate the transfer function model derived above, a 0.19 nTpp sine wave at different frequencies is applied along x-axis and y-axis respectively, and the amplitude frequency and phase frequency responses are recorded. As shown in Fig.3 a), the amplitude-frequency responses to B_x field are shown in open circles, and the solid line is the fitted curve according to (14). The phase-frequency response is shown in Fig.3 b). The phase response predicted using the fitted model (solid line) agrees very well with the experimental results (open circles). For comparison, the fitted frequency responses using the model proposed in [13] are also shown in dot dashed lines. It is apparent that the model fails to characterize the field frequency responses in low frequency domain. The actual amplitude response is 25 times larger than that predicted with previous models. This will result in the underestimate of the rotation measurement error caused by low-frequency magnetic noise. As mentioned above, the difference between the model in this work and that in previous works is that the non-zero R_{tot}^n has not been ignored in the derivation process of magnetic field transfer functions. The experimental results here verified that how to deal with R_{tot}^n really makes a difference. The frequency responses to B_y field are shown in Fig.4. The experimental data (open squares) are in consistency with the fitted curves (dashed line) using (18). Comparison between the theoretical results and the experimental results shows that the theoretical model in this work has excellent rationality. And a summary of the fitted values of the variables is listed in Table 1. When $\omega > \omega_1$, the SERFCM exhibits responses like a magnetometer. This is because that the noble gas cannot respond so quickly for its small relaxation rate, and the spin ensembles are decoupled.
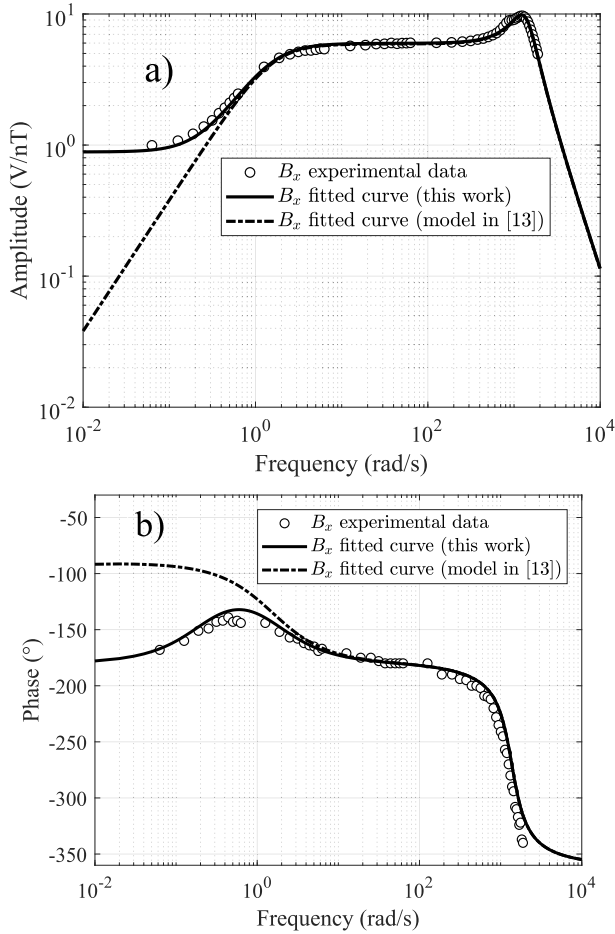
FIGURE 3. Frequency response to B_x field. (a) Amplitude frequency response. (b) Phase frequency response.

FIGURE 4. Frequency response to B_y field. (a) Amplitude frequency response. (b) Phase frequency response.

TABLE 1. Fitted values of the variables in $G_{Bx}(s)$ and $G_{By}(s)$.

Variables	Value (rad/s)
Γ_1	-1.551
ω_1	0.169
Γ_2	-439.663
ω_2	1299.332
z_{Bx1}	-0.232
z_{Bx2}	-1.551
z_{By1}	-5×10^{-6}
z_{By2}	-0.301
z_{By3}	-445.189

As a result, there is a resonance peak corresponding to the alkali-metal response at ω_2. When $z_{Bx1} \leqslant \omega \leqslant \omega_1$, the SERFCM exhibits its self-compensate characteristics as predicted in previous models. When $0 \leqslant \omega < z_{Bx1}$, the amplitude frequency response to B_x reaches a constant value, which can be predicted by our model. And the absolute values of z_{Bx1} and z_{By2} indicate a R_{tot}^n of about 0.27 rad/s, much larger than the adopted values in previous works. In addition to quadrupolar relaxation, the larger relaxation rate is thought to be caused by the magnetic field gradient felt by the nuclear spins.

The dynamical responses to transverse magnetic fields are also experimentally studied to check the validity of the model and its theory. A step B_x magnetic field of 0.094 nT is applied to the system, the magnetic field signal and the co-magnetometer output are recorded simultaneously at a sampling rate of 200 Hz by the data acquisition system during a period 200 seconds. The recorded magnetic signal is used as the input signal of the simulation model established on the fitted variables in Table 1. Then the simulation output and the co-magnetometer out are compared in time domain. The step B_y response is compared in the same way described above. As is shown in Fig.5 a), the simulation output in red
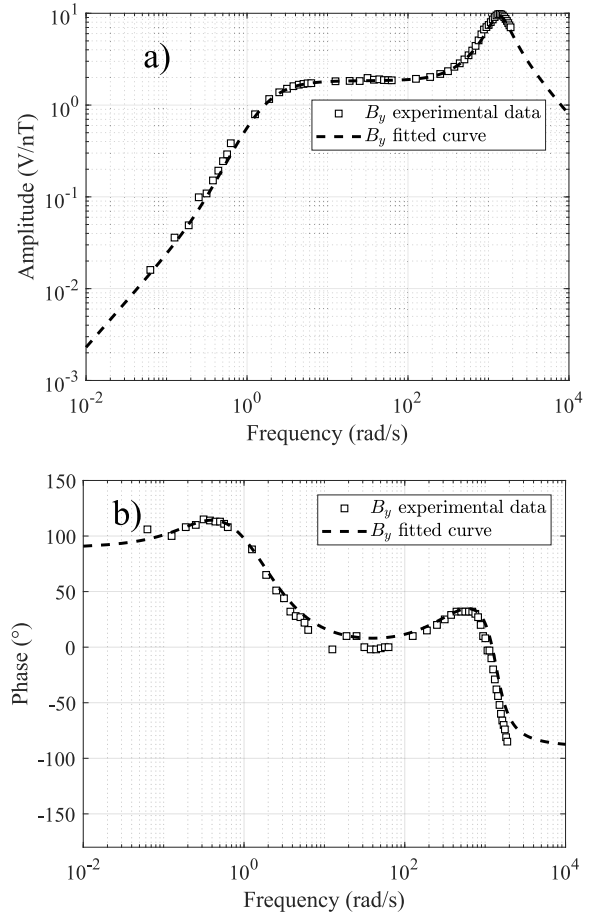
line provides a good dynamical response predication of the co-magnetometer output to B_x in black open circles, proving the accuracy of fitted model. Although the step response comparison to B_y shown in Fig.5 b) exhibits some mismatch at the very beginning of the step signal, the steady state response converges approximately to zero, which is consistent with theoretical analysis. The mismatch comes from the error of the fitted $G_{By}(s)$. As is shown in Fig.3 and Fig.4, the amplitude response to B_y is much smaller than that to B_x, and therefore the noise of the probe system introduces more error in $G_{By}(s)$.

The validity of the model and its theory has been confirmed by simulation and experimental results above. The unexpected sensitivity of the co-magnetometer to B_x field
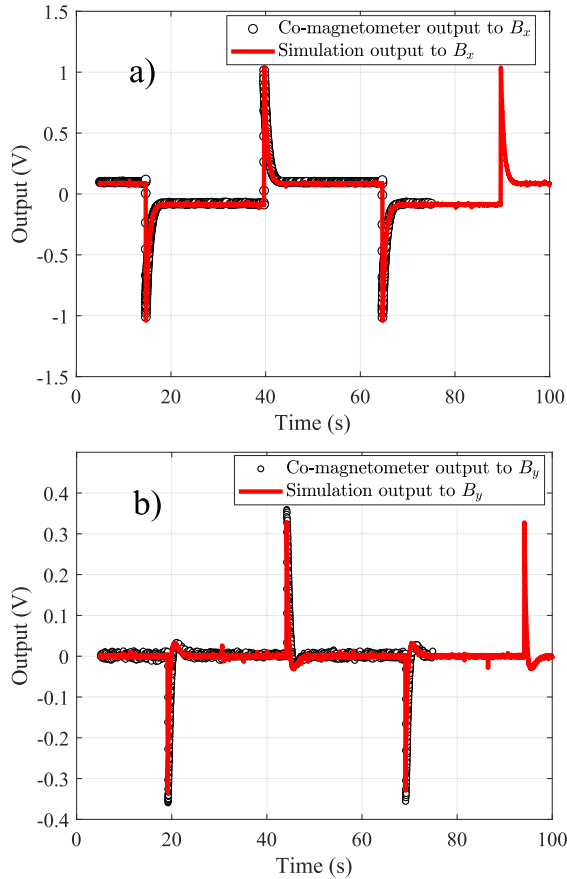
FIGURE 5. Comparison between experimental results and simulation results. (a) B_x step response. (b) B_y step response.

can be explained by analyzing the steady state solution of the nuclear polarization to transverse magnetic field inputs. At the compensation point, the net magnetic field experienced by the alkali-metal atoms is close to zero. The alkali-metal atoms will operate as a high-sensitivity SERF magnetometer that is primarily sensitive to the total field along y-axis $\tilde{B}_y$. If an external perturbation B_y field applies, the nuclear polarization projection on y-axis $P_y^n = -B_y/(\lambda M^n)$. The total field felt by the alkali-metal atoms is $\tilde{B}_y = B_y + \lambda M^n P_y^n = B_y - B_y = 0$. That is to say, the nuclear magnetization rotates to follow the changes in external B_y field, canceling its effect on the alkali-metal. If an external perturbation B_x field applies, the nuclear polarization projection on y-axis $P_y^n = -R_{tot}^n B_x/(B^n \gamma^n \lambda M^n)$. The total field felt by the alkali-metal atoms is $\tilde{B}_y = \lambda M^n P_y^n = -R_{tot}^n B_x/(\gamma^n B^n)$. Clearly, the alkali-metal spins will respond to the residual $\tilde{B}_y$ field if R_{tot}^n considered non-zero.

IV. CONCLUSION

In conclusion, we analyzed the magnetic field response model of a K-Rb-^{21}Ne SERFCM based on the state space method. Different from the model proposed ever before, the model in this work indicates that the non-zero nuclear spin relaxation rate R_{tot}^n will introduce a non-zero zero point in the transverse magnetic field transfer functions, aggravating the influence of the low frequency transverse magnetic field components, especially for the B_x component. The results of the experimental data analysis and theory study are in consistency. Combined with stochastic process analysis methods, the model here will provide an accurate and effective way to estimate the rotation measurement error induced by magnetic noise. This study provides us a better understanding on the self-compensation characteristic in SERFCM and inspires us to explore novel nuclear spin manipulation methods of reducing the relaxation of nuclear spins.

REFERENCES

[1] S. K. Lamoreaux, J. P. Jacobs, B. R. Heckel, F. J. Raab, and E. N. Fortson, "New limits on spatial anisotropy from optically-pumped $sup201$ Hg and ^{199}Hg," *Phys. Rev. Lett.*, vol. 13, no. 1, p. 3125, Dec. 1986.

[2] C. A. Baker et al., "Improved experimental limit on the electric dipole moment of the neutron," *Phys. Rev. Lett.*, vol. 97, no. 13, Sep. 2006, Art. no. 131801.

[3] M. Smiciklas, J. M. Brown, L. W. Cheuk, S. J. Smullin, and M. V. Romalis, "New test of local Lorentz invariance using a ^{21}Ne-Rb-K comagnetometer," *Phys. Rev. Lett.*, vol. 107, Oct. 2011, Art. no. 171604.

[4] J. M. Brown, S. J. Smullin, T. W. Kornack, and M. V. Romalis, "New limit on lorentz- and CPT-violating neutron spin interactions," *Phys. Rev. Lett.*, vol. 105, no. 15, Oct. 2010, Art. no. 151604.

[5] G. Vasilakis, J. M. Brown, T. W. Kornack, and M. V. Romalis, "Limits on new long range nuclear spin-dependent forces set with a k-^{3}He comagnetometer," *Phys. Rev. Lett.*, vol. 103, no. 26, p. 261801, 2009.

[6] M. Bulatowicz et al., "Laboratory search for a long-range T-odd, P-odd interaction from axionlike particles using dual-species nuclear magnetic resonance with polarized ^{129}Xe and ^{131}Xe Gas," *Phys. Rev. Lett.*, vol. 111, no. 10, Sep. 2013, Art. no. 102001.

[7] E. Kanegsberg, "A nuclear magnetic resonance (NMR) gyro with optical magnetometer detection," *Proc. SPIE*, vol. 157, pp. 73–81, Dec. 1978.

[8] E. A. Donley, "Nuclear magnetic resonance gyroscopes," in *Proc. IEEE Sensors Conf.*, Nov. 2010, pp. 17–22.

[9] M. Larsen and D. Meyer, "Nuclear magnetic resonance gyro for inertial navigation," *Gyroscopy Navigat.*, vol. 5, no. 2, pp. 75–82, Apr. 2014.

[10] T. G. Walker and M. S. Larsen, "Spin-exchange-pumped NMR gyros," *Adv. At., Mol., Opt. Phys.*, vol. 65, 2016, pp. 373–401.

[11] A. K. Vershovskii, A. S. Pazgalev, and V. I. Petrov, "The nature of the effect of precession-frequency mismatch between ^{129}Xe and ^{131}Xe nuclei under spin-exchange pumping by alkali-metal atoms," *Tech. Phys. Lett.*, vol. 44, no. 4, pp. 313–315, 2018.

[12] T. W. Kornack and M. V. Romalis, "Dynamics of two overlapping spin ensembles interacting by spin exchange," *Phys. Rev. Lett.*, vol. 89, no. 25, p. 253002, Dec. 2002.

[13] T. W. Kornack, R. K. Ghosh, and M. V. Romalis, "Nuclear spin gyroscope based on an atomic comagnetometer," *Phys. Rev. Lett.*, vol. 95, no. 23, Nov. 2005, Art. no. 230801.

[14] J. Fang, J. Qin, S. Wan, Y. Chen, and R. Li, "Atomic spin gyroscope based on ^{1}29Xe-Cs comagnetometer," *Chin. Sci. Bull.*, vol. 58, no. 13, pp. 1512–1515, 2013.

[15] J. Fang, S. Wan, and H. Yuan, "Dynamics of an all-optical atomic spin gyroscope," *Appl Opt*, vol. 52, no. 30, pp. 7220–7227, Oct. 2013.

[16] R. Li, W. Fan, L. Jiang, L. Duan, W. Quan, and J. Fang, "Rotation sensing using a K-Rb-^{21}Ne comagnetometer," *Phys. Rev. A, Gen. Phys.*, vol. 94, no. 3, 2016, Art. no. 032109.

[17] L. Jiang et al., "Suppression of the cross-talk effect in a dual-axis K-Rb-^{21}Ne comagnetometer," *Phys. Rev. A, Gen. Phys.*, vol. 95, no. 6, 2017, Art. no. 062103.

[18] L. Duan et al., "Rotation sensing decoupling of a dual-axis K-Rb-^{21}Ne atomic comagnetometer," *Appl. Opt.*, vol. 57, no. 7, pp. 1611–1616, 2018.

[19] L. Jiang et al., "A parametrically modulated dual-axis atomic spin gyroscope," *Appl. Phys. Lett.*, vol. 112, no. 5, 2018, Art. no. 054103.

[20] M. E. Limes, D. Sheng, and M. V. Romalis, "^{3}He-^{1}29Xe comagnetometery using ^{8}7Rb detection and decoupling," *Phys. Rev. Lett.*, vol. 120, no. 3, 2018, Art. no. 033401.
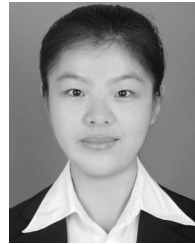
[21] Y. Chen *et al.*, ''Spin exchange broadening of magnetic resonance lines in a high-sensitivity rotating K-Rb-^{21}Ne co-magnetometer,'' *Sci. Rep.*, vol. 6, Nov. 2016, Art. no. 36547.

[22] R. Li, W. Quan, W. Fan, L. Xing, and J. Fang, ''Influence of magnetic fields on the bias stability of atomic gyroscope operated in spin-exchange relaxation-free regime,'' *Sens. Actuators A, Phys.*, vol. 266, pp. 130–134, Oct. 2017.

[23] J. Fang *et al.*, ''Low frequency magnetic field suppression in an atomic spin co-magnetometer with a large electron magnetic field,'' *J. Phys. B, At. Mol. Opt. Phys.*, vol. 49, no. 6, 2016, Art. no. 065006.

[24] S. R. Schaefer, G. D. Cates, T.-R. Chien, D. Gonatas, W. Happer, and T. G. Walker, ''Frequency shifts of the magnetic-resonance spectrum of mixtures of nuclear spin-polarized noble gases and vapors of spin-polarized alkali-metal atoms,'' *Phys. Rev. A, Gen. Phys.*, vol. 39, no. 11, pp. 5613–5623, 1989.

[25] Y. Chen, W. Quan, L. Duan, Y. Lu, L. Jiang, and J. Fang, ''Spin-exchange collision mixing of the K and Rb ac Stark shifts,'' *Phys. Rev. A, Gen. Phys.*, vol. 94, no. 5, 2016, Art. no. 052705.

[26] L. Duan, J. Fang, R. Li, L. Jiang, M. Ding, and W. Wang, ''Light intensity stabilization based on the second harmonic of the photoelastic modulator detection in the atomic magnetometer,'' *Opt Express*, vol. 23, no. 25, pp. 32481–32489, Dec. 2015.

[27] W. Quan, Q. Wang, and Y. Zhai, ''A dual closed-loop drive and control system of photoelastic modulator for atomic magnetometer,'' *Meas. Sci. Technol.*, vol. 29, no. 6, 2018, Art. no. 065105.

WEIJIA ZHANG received the B.S. degree in electronic information engineering and the M.S. degree in optical engineering from Yanshan University, China, in 2014 and 2017, respectively. She is currently pursuing the Ph.D. degree with the School of Instrumentation and Optoelectronic Engineering, Beihang University. Her current research interest includes the atomic spin precession signal detection methods of atomic spin sensors.
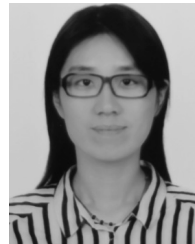
WENFENG FAN received the B.S. degree in mechanical engineering from Shandong University, China, in 2012. He is currently pursuing the Ph.D. degree with the School of Instrumentation and Optoelectronic Engineering, Beihang University. His research interest includes the magnetic response of atomic magnetometers and co-magnetometers operated in the spin-exchange relaxation-free regime.

LI XING received the B.S. degree in measurement and control technology and instruments from Harbin Engineering University, Harbin, China, in 2015. She is currently pursuing the Ph.D. degree with the School of Instrumentation and Optoelectronic Engineering, Beihang University. Her current research interests include the closed-loop control technology and error compensation technology of the atomic magnetometers/co-magnetometers operated in the spin-exchange relaxation free regime.

WEI QUAN received the Ph.D. degree from Beihang University, in 2008, where he is currently a Professor with the School of Instrumentation and Optoelectronic Engineering, Beihang University. His research interests include celestial navigation and the recently developed atomic inertial sensors based on an alkali-metal vapor cell.

GANG LIU received the B.S. and M.S. degrees from Shandong University, China, in 1992 and 1998, respectively, and the Ph.D. degree from the Dalian University of Technology, China, in 2001. He is currently a Ph.D. Supervisor with the School of Instrumentation and Optoelectronic Engineering, Beihang University. His research interests include magnetic suspension technology, spacecraft attitude control, and high-sensitivity atomic magnetometers.

● ● ●